Link to published version (if available):
10.1121/10.0000615

Link to publication record in Explore Bristol Research
PDF-document

University of Bristol - Explore Bristol Research
General rights

Higher-order spatial correlation coefficients of ultrasonic backscattering signals using partial cross-correlation analysis

Yongfeng Song, Christopher M. Kube, Jie Zhang, and Xiongbing Li

ARTICLES YOU MAY BE INTERESTED IN

Ultrasonic diffraction by a circular transducer: Isogeometric analysis sensitivity to full Gauss quadrature points
The Journal of the Acoustical Society of America **147**, EL74 (2020); https://doi.org/10.1121/10.0000591

Tracking of multiple surface vessels based on passive acoustic underwater arrays
The Journal of the Acoustical Society of America **147**, EL87 (2020); https://doi.org/10.1121/10.0000598

Robust far-field subwavelength imaging of scatterers by an acoustic superlens
The Journal of the Acoustical Society of America **146**, 4131 (2019); https://doi.org/10.1121/1.5134780

Cross-linguistic f0 differences in bilingual speakers of English and Korean
The Journal of the Acoustical Society of America **147**, EL67 (2020); https://doi.org/10.1121/10.0000498

Superposition method for modelling boundaries between media in viscoelastic finite difference time domain simulations
The Journal of the Acoustical Society of America **146**, 4382 (2019); https://doi.org/10.1121/1.5139221

Green's function approach for the transmission loss of concentrically multi-layered circular dissipative chamber
The Journal of the Acoustical Society of America **147**, 867 (2020); https://doi.org/10.1121/10.0000675

Higher-order spatial correlation coefficients of ultrasonic backscattering signals using partial cross-correlation analysis

Yongfeng Song,[1] Christopher M. Kube,[2] Jie Zhang,[3] and Xiongbing Li[1,a]

[1]*School of Traffic and Transportation Engineering, Central South University, Changsha, Hunan 410075, China*

[2]*Department of Engineering Science and Mechanics, Penn State University, University Park, Pennsylvania 16802, USA*

[3]*Department of Mechanical Engineering, University of Bristol, Bristol BS8 1TR, United Kingdom*

ABSTRACT:

The spatial correlation properties of ultrasonic backscattering signals in random media have important implications. For example, they can be used for microstructural characterization and flaw detection in engineering materials. However, the traditional spatial correlation coefficient (SCC) is only a leading order quantity that does not capture the true spatial correlations of random media. This is caused by neglecting confounding variables such as non-zero means or other non-zero odd-order moments. Here, the SCC is generalized from zeroth- to general-order through partial cross-correlation analysis. A series of indicators are defined to quantify the SCC curve at zero time lag, and the maximum time shift curve, which are both functions of lateral separation between two sensor positions. A stainless-steel specimen and a focused ultrasonic transducer are used to verify the method. Scattering measurements show that the higher-order SCC can consistently capture spatial correlations whereas the zeroth-order SCC is inadequate. The zeroth-order SCC is shown to predict a step size that can be more than six times too large. Thus, the present method can provide better understanding of statistical correlations and conditions to measure uncorrelated backscattering signals. © 2020 Acoustical Society of America. https://doi.org/10.1121/10.0000615

I. INTRODUCTION

Scattering of ultrasound from grain boundaries in metals, often referred to as ultrasonic backscattering, has been widely used in microstructural characterization[1–3] and microscale flaw detection.[4–6] A backscattering signal typically has a spatially dependent random character stemming from randomness on the microscale, e.g., random grain orientations. However, spatial correlations do exist. For example, backscattering measurements captured at two spatial locations can appear nearly identical if the two spatial locations are close enough. The notion of *close enough* depends on a spatial length characteristic related to the heterogeneity.[7,8] Thus, measurements of the spatial correlations in backscattering signals could provide important insight into the degree of material heterogeneity or mechanical property fluctuations. The spatial correlations then have many potential applications including detecting multiple-scattering behavior,[9,10] evaluating material microstructure,[8,11] and testing for flaws within the volume of a part.[12–14] The key to applying spatial correlations of backscattering signals in practical scenarios is to assess their degree of similarity.

The measurement of spatial correlation of backscattering signals is closely related to the problem of coherence in optics. Research on optical coherence stems back to the late 19th century.[15,16] In the early 20th century, Van Cittert[17,18] and Zernike[19] built the basics for the coherence of optical waves, which explains the increase of coherence area with propagation distance from the source. Their contributions formed the foundation of the Van Cittert–Zernike theorem.[20] Then, Wolf developed a mutual coherence function to simultaneously calculate the degree of temporal and spatial coherence.[21,22] In fact, Wolf's mutual coherence function is known as the cross-correlation analysis of optical waves. In the late 20th century, Derode and Fink introduced the notion of coherence into acoustics. They used a phase array ultrasonic transducer to perform experimental measurements of coherence via the spatial correlation coefficient (SCC) of backscattered signals.[23]

Later, Fink and his co-workers provided many advances to the topic.[9–12,23–25] For instance, anisotropic materials, such as cross-ply composites, were characterized by SCC curves.[9,24] Additionally, they developed a backscatter tensor imaging method for evaluating anisotropic soft tissues with SCC curves.[25] In these cases,[24,25] a complete measurement model that incorporated material effects and the experimental apparatus was not given. In the area of ultrasonics, Thompson *et al.*[7,8] modeled the combined effects of the measurement system and polycrystalline microstructure and predicted SCC curves of ultrasonic backscattering. This model showed the SCC curve can be strongly influenced by the measurement system, the specimen's microstructural statistics, and an overlap integral of the sound field.[8] In applications, Thompson's SCC model can be used to fit experimental measurements of SCC and obtain microstructural information such as the average grain size.

a)Electronic mail: lixb_ex@163.com

An impediment to Thompson's method was the inability to account for backscattering measurements that have non-zero odd-order moments, which is common in measurements involving low-frequency Rayleigh scattering. Neglecting non-zero odd-order moments when they are present can cause one to unnecessarily increase the separation distance between the sensors, which sacrifices spatial resolution. To remedy this issue, partial correlation analysis can be used, which can quantify the correlation between two variables under conditioning on one or more variables and can provide higher-order correlation coefficients.[26,27] For example, Stark et al.[28] has extended a partial cross-correlation analysis method to estimate linear correlations between neural activity and several other interdependent features at multiple time lags in neuroscience. However, to the best of authors' knowledge, the partial correlation analysis method has not been applied to ultrasonic backscattering yet.

In this work, the zeroth-order SCC is extended to higher-order to correctly assess the SCC of ultrasonic back-scattered signals in polycrystalline materials. First, the concepts of partial cross-correlation analysis will be introduced into spatial correlation statistics by considering the non-zero odd-order moments belonging to the ensemble of ultrasonic signals. Then, the higher-order SCC curve without time lag and the maximum time shift curve are defined as functions of lateral separation between two transducer positions. Several indicators are given to quantify these two kinds of curves, which help to choose a proper separation distance in scattering measurements. The present method is verified by the ultrasonic scattering measurements performed on a stainless-steel specimen. The higher-order SCC is analyzed with and without time lag and the effects of the measurement system is discussed. Last, analysis of the high-order SCC curve is used to determine optimal indicators to estimate the minimal separation distance for resolving uncorrelated backscattering signals.

II. METHOD

A. Partial cross-correlation analysis

Suppose a set of N time-amplitude (voltage) ultrasonic waveforms is acquired using a typical ultrasonic scanning procedure, as described in Ref. 3. Contained within each signal is a contribution caused by scattering from the polycrystalline microstructure along with any coherent reflections from sample surfaces. The microstructure is assumed to be locally heterogeneous, but homogeneous on average (an assumption of statistical homogeneity). Let $V_{\mathbf{x}}(t)$ and $V_{\mathbf{x}'}(t)$ be two signals contained in the set that were acquired at position $\mathbf{x}$ and $\mathbf{x}'$. The spatial cross-correlation of the microstructural scattering within a time gate from t_0 to t_1 as[14]

$$SCC(\tau|V_{\mathbf{x}},V_{\mathbf{x}'}) = \frac{\int_{t_0}^{t_1} V_{\mathbf{x}}(t) \cdot V_{\mathbf{x}'}(t-\tau-\kappa_{\mathbf{xx}'})\mathrm{d}t}{\sqrt{\int_{t_0}^{t_1}[V_{\mathbf{x}}(t)]^2\mathrm{d}t \cdot \int_{t_0}^{t_1}[V_{\mathbf{x}'}(t-\kappa_{\mathbf{xx}'})]^2\mathrm{d}t}}, \tag{1}$$

where τ is the time lag and $\kappa_{\mathbf{xx}'}$ is an alignment factor that accounts for possible misalignment in the experimental configuration. When there is no time lag ($\tau = 0$), Eq. (1) is the form defined by Thompson et al.[7] and Yu et al.[8] The time lag τ is employed to account for phase variations in the backscattering signal. In an application similar to that of Ref. 29 on seismic data, the alignment factor $\kappa_{\mathbf{xx}'}$ provides an adjustment when the travel path between the transducer and sample varies, for example, when the specimen has a curved surface. In a normal incident setup, $\kappa_{\mathbf{xx}'}$ can be measured from analyzing the arrival times of front-wall echoes. In practice, Eq. (1) is calculated using its discrete form.

The spatial average or first-order raw moment of the set of signals is denoted $\langle V(t) \rangle$. More generally, the odd-order raw moments of the signals are explicitly

$$\langle V^{2n-1}(t) \rangle = \frac{1}{N}\sum_{i=1}^{N}\left[V_i^{2n-1}(t)\right], \tag{2}$$

where $n = 1, 2, 3, \dots$ and $i = 1, 2, \dots, N$. The odd-order raw moments are important to the SCC because the traditional SCC model as that given in Eq. (1) is only appropriate when $\langle V^{2n-1}(t) \rangle = 0$. Thus, the SCC in Eq. (1) is referred to as the zeroth-order spatial correlation coefficient and the higher-order SCC has not be defined or applied to scattering signals. Thus, our goal is to quantify and eliminate adverse effects of the non-zero odd-order raw moments, i.e., $\langle V^{2n-1}(t) \rangle \neq 0$, on the spatial correlations using a partial cross-correlation analysis.

In the area of statistics, it is well-known that using the zeroth-order correlation coefficient will give misleading results when one or more confounding variables associated with the variables of interest exist.[27] Here, the confounding variable is understood as an extraneous variable that influences both the dependent variable and independent variable, causing a spurious association. Thus, taking the first moment $\langle V(t) \rangle$ into account, the first-order SCC can be found as

$$SCC(\tau|V_{\mathbf{x}},V_{\mathbf{x}'},\langle V \rangle)$$
$$= \frac{SCC(\tau|V_{\mathbf{x}},V_{\mathbf{x}'}) - SCC(\tau|V_{\mathbf{x}},\langle V \rangle)SCC(0|V_{\mathbf{x}'},\langle V \rangle)}{\sqrt{1-[SCC(\tau|V_{\mathbf{x}},\langle V \rangle)]^2}\sqrt{1-[SCC(0|V_{\mathbf{x}'},\langle V \rangle)]^2}}, \tag{3}$$

where $SCC(\tau|V_{\mathbf{x}},\langle V \rangle)$ and $SCC(0|V_{\mathbf{x}'},\langle V \rangle)$ are calculated from Eq. (1). This equation is based on Eq. (8) of Ref. 28 (with the two-dimensional time delays reduced into one with $\tau_1 = \tau_2 = \tau$). If $\langle V(t) \rangle = 0$, then $SCC(\tau|V_{\mathbf{x}},\langle V \rangle) = SCC(0|V_{\mathbf{x}'},\langle V \rangle) = 0$, so that $SCC(\tau|V_{\mathbf{x}},V_{\mathbf{x}'},\langle V \rangle)$ recovers the traditional or zeroth-order form of $SCC(\tau|V_{\mathbf{x}},V_{\mathbf{x}'})$. Thus, $SCC(\tau|V_{\mathbf{x}},V_{\mathbf{x}'},\langle V \rangle)$ is a more general expression of $SCC(\tau|V_{\mathbf{x}},V_{\mathbf{x}'})$ for the case when $\langle V(t) \rangle \neq 0$. Note that the physical meaning of the spatial correlation goes unchanged. Another form of first-order SCC can also be defined. For example, $SCC(\tau|V_{\mathbf{x}},V_{\mathbf{x}'},\langle V^3 \rangle)$ is formed by replacing $\langle V \rangle$ with $\langle V^3 \rangle$ in Eq. (3).

758   J. Acoust. Soc. Am. **147** (2), February 2020

Song *et al.*

Additionally, the present method, based on the partial cross-correlation analysis, is able to account for effects of additional confounding variables on the correlation

coefficient. For example, the influence of the confounding variables $\langle V \rangle$ and $\langle V^3 \rangle$ results in the second-order SCC are

$$SCC\big(\tau|V_{\mathbf{x}}, V_{\mathbf{x}'}, \langle V \rangle, \langle V^3 \rangle\big) = \frac{SCC(\tau|V_{\mathbf{x}}, V_{\mathbf{x}'}, \langle V \rangle) - SCC\big(\tau|V_{\mathbf{x}}, \langle V^3 \rangle, \langle V \rangle\big) SCC\big(0|V_{\mathbf{x}'}, \langle V^3 \rangle, \langle V \rangle\big)}{\sqrt{1 - [SCC(\tau|V_{\mathbf{x}}, \langle V^3 \rangle, \langle V \rangle)]^2} \sqrt{1 - [SCC(0|V_{\mathbf{x}'}, \langle V^3 \rangle, \langle V \rangle)]^2}}. \quad (4)$$

Note that Eq. (4) is rather cumbersome as it contains three first-order SCCs, and six zeroth-order SCCs. Similarly, higher-order SCC can be calculated to eliminate the confounding effects from combinations of $\langle V \rangle$, $\langle V^3 \rangle$, …, $\langle V^{2n-1}(t) \rangle$, by using the recursive formula of partial cross-correlation analysis.[26,28] In some cases, the higher-order corrections are small and can be neglected. The need to extend to a certain order and the convergence of SCC are discussed in Secs. III B and III C.

B. Indicator analysis of SCC

In the present work, indicators will be defined to give characteristic length scales related to the general-order SCC. The first indicator is the noise spatial correlation length (NSCL) as defined by Thompson et al.[7] and Yu et al.[8] Supposing the lateral separation between transducer position $V_{\mathbf{x}}$ and $V_{\mathbf{x}'}$ is $|\mathbf{x} - \mathbf{x}'|$, the average $SCC(\tau = 0||\mathbf{x} - \mathbf{x}'|)$ can be calculated using many pairs of $V_{\mathbf{x}}$ and $V_{\mathbf{x}'}$ with the same $|\mathbf{x} - \mathbf{x}'|$. The NSCL is obtained by the following equation as

$$SCC\big(0||\mathbf{x} - \mathbf{x}'| = NSCL\big) = 1/e, \quad (5)$$

which denotes the point where the SCC drops by the fraction $SCC = 1/e$. The NSCL can be regarded as a shape factor or scaling factor of the SCC curve.

The NSCL cannot provide a minimum lateral separation distance to guarantee a pair of backscattering signals to be uncorrelated, which is important when designing an ultrasonic scattering measurement.[6] Rather, the Student's t-test is used as such a criterion.[30] The null hypothesis H_0 is $V_{\mathbf{x}}(t)$ and $V_{\mathbf{x}'}(t)$ are uncorrelated; and the alternate hypothesis H_1 is $V_{\mathbf{x}}(t)$ and $V_{\mathbf{x}'}(t)$ are correlated. Accept H_0 when the test statistic satisfies

$$-\sqrt{\frac{[t_\alpha(M-2)]^2}{(M-2) + [t_\alpha(M-2)]^2}}$$
$$\leq SCC\big(0||\mathbf{x} - \mathbf{x}'|\big) \leq \sqrt{\frac{[t_\alpha(M-2)]^2}{(M-2) + [t_\alpha(M-2)]^2}}, \quad (6)$$

where $t_\alpha(M-2)$ is the Student's t-distribution[30] with the significance level α. The $M-2$ is the degrees of freedom, and M is the number of independent sampling points of the waveforms, which will be used to calculate the SCC with

the discrete form of Eq. (1). This independent data assumption will fail if an excessive sampling rate is used. The effects of sampling rate on the SCC will be discussed in Sec. III D. Oppositely, accept H_1 if the test statistic falls outside of the bounds in Eq. (6). The second indicator is defined as the upper bound in Eq. (6) and denotes it as the uncorrelated transducer distance (UTD), i.e.,

$$SCC\big(0||\mathbf{x} - \mathbf{x}'| = UTD\big) = \sqrt{\frac{[t_\alpha(M-2)]^2}{(M-2) + [t_\alpha(M-2)]^2}}. \quad (7)$$

It should be noted that, if α is too high, the type II error of hypothesis testing is inevitable. Further, uncorrelation is only a necessary condition of independence. Yet, UTD remains a valuable indicator in applications to provide the smallest scanning step in ultrasonic measurements.

The third indicator for $SCC(0||\mathbf{x} - \mathbf{x}'|)$ is the first zero point (FZP). It can be given by the inverse function of SCC as

$$SCC\big(0||\mathbf{x} - \mathbf{x}'| = FZP\big) = 0. \quad (8)$$

However, FZP is always too large to be used as the scanning step as to be shown in Sec. III E. The indicators NSCL, UTD, and FZP are both the spatial indicators about the lateral separation $|\mathbf{x} - \mathbf{x}'|$. Thus, the number of pairs of $V_{\mathbf{x}}(t)$ and $V_{\mathbf{x}'}(t)$ for averaging $SCC(0||\mathbf{x} - \mathbf{x}'|)$ will affect the estimated accuracy of the three indicators. For brevity, this point is not included in this paper, but we suggest using as many pairs of waveforms as possible.

Additional three indicators can be defined for the higher-order SCC with time lag. The maximum time lag can be defined as

$$\tau_{\max}(V_{\mathbf{x}}, V_{\mathbf{x}'}) = \arg \max_\tau |SCC(\tau|V_{\mathbf{x}}, V_{\mathbf{x}'})|,$$
$$\tau_{\max}(V_{\mathbf{x}}, V_{\mathbf{x}'}, \langle V \rangle) = \arg \max_\tau |SCC(\tau|V_{\mathbf{x}}, V_{\mathbf{x}'}, \langle V \rangle)|,$$
$$\tau_{\max}\big(V_{\mathbf{x}}, V_{\mathbf{x}'}, \langle V \rangle, \langle V^3 \rangle\big)$$
$$= \arg \max_\tau |SCC\big(\tau|V_{\mathbf{x}}, V_{\mathbf{x}'}, \langle V \rangle, \langle V^3 \rangle\big)|. \quad (9)$$

J. Acoust. Soc. Am. **147** (2), February 2020

Song et al.   759

Again, one can replace $\tau_{\max}(V_{\mathbf{x}}, V_{\mathbf{x}'}, \langle V \rangle)$ with $\tau_{\max}(V_{\mathbf{x}}, V_{\mathbf{x}'}, \langle V^3 \rangle)$ similar to Eq. (3). Note that although there are absolute value signs in Eq. (9), some results from the argmax function could be negative, and their absolute values give the corresponding maximum time shift. Considering the lateral separation $|\mathbf{x} - \mathbf{x}'|$, the average maximum time shift (MTS) curve $|\tau_{\max}(|\mathbf{x} - \mathbf{x}'|)|$ can be given by using many pairs of $V_{\mathbf{x}}$ and $V_{\mathbf{x}'}$. Then, a sigmoid function can be utilized to fit the MTS curve as

$$\min \| |\tau_{\max}(|\mathbf{x} - \mathbf{x}'|)| - s(|\mathbf{x} - \mathbf{x}'|) \|_2 ,$$
$$s(x) = 1/(a + b \cdot x^{-L}),$$
$$\text{s.t. } a > 0, \quad b > 0, \quad L > 0, \quad (a, b, L) \in \mathbb{R}, \tag{10}$$

where a, b, and L are the fitting coefficients, and $\| \bullet \|_2$ means the calculation of the l_2 norm, i.e., the square root of the sum of squared errors. The third derivative of the sigmoid function $s(x)$ can be given as

$$\frac{d^3 s}{dx^3} = \frac{bLx^{L-3}\left[a^2(L+1)(L+2)x^{2L} - 4ab(L^2 - 1)x^L + b^2(L-2)(L-1)\right]}{(ax^L + b)^4}. \tag{11}$$

The third derivative of $s(x)$ has three extremums, which are found through a numerical search algorithm. These three indicators are named as the first, second, and third extremum of derivative function, and notated as EODF1, EODF2, and EODF3, respectively. They are not only spatial indicators about the lateral separation $|\mathbf{x} - \mathbf{x}'|$, but also temporal indicators about the time shift τ.

In the present application, we will use these six indicators to help answer the question in Ref. 12 related to how far apart must two positions be to receive uncorrelated information using a single ultrasonic focused transducer. Experimental results for different indicators are given in Sec. III E. The higher-order SCC model developed above will be utilized to fit the experimental curves of $SCC(0||\mathbf{x} - \mathbf{x}'|)$ and $|\tau_{\max}(|\mathbf{x} - \mathbf{x}'|)|$ to extract these indicators for practical applications.

III. EXPERIMENTAL RESULTS

A. Data acquisition

In this section, ultrasonic scattering measurements are performed to compare the various orders of SCC. A 304 stainless steel specimen is used because of its relatively simple microstructure, which was found to contain untextured and equiaxed single phase grains on average. The dimensions of the specimen are 100 mm × 40 mm × 15 mm. Based on ASTM metallurgical standard E112,[5] the average grain diameter was measured as $\bar{d} = 44.2 \pm 2.8 \, \mu\text{m}$ using optical microscopy.

The scattering measurements were performed with a single focused immersion style transducer. Without loss of generality to the various modes of scattering, the longitudinal-to-longitudinal scattering is measured using a pulse-echo configuration at normal incidence to the top surface of the specimen. The immersion ultrasonic scanning system, shown in Fig. 1, consists of a water tank, a computer-controlled micropositioning system, a JSR DPR-300 pulser/receiver, and an ADLink 200 MHz data acquisition card (digitizer). The longitudinal wave velocities of the water and the specimen are assumed to be 1486 m/s and 5750 m/s,

respectively. The pertinent transducer properties are given in Table I.

The spot sizes of the focused transducers are included in Table I, for comparison between the spot sizes (-6 dB beam diameter) and the indicators in Sec. III E. A normalized wavenumber is defined as $k_L \bar{d}$ to indicate the dependence on the wave number or grain size.[31] Table I also shows $k_L \bar{d}$ for each frequency. The scattering mean free paths are measured as $1/(2\alpha_L)$, where α_L are the longitudinal attenuation coefficients at central frequencies from the different transducers.[31,32] Since the longitudinal attenuation is proportional to $k_L \bar{d}$, the mean free path is inversely proportional to $k_L \bar{d}$. The mean free paths give an indication of possible multiple scattering effects in the signals.[31,32] Multiple scattering is presumed to be weak for the present configurations since the mean free paths are more than an order of magnitude greater than the spot size in the material. Furthermore, for transducers C and D, the mean free paths are greater than the travel distance 30 mm (back and forth) within the specimen.

B-scans are conducted by using each transducer and a scanning step of 0.1 mm. The material paths (focal depth below the interface) are kept fixed at 7 mm, which is smaller
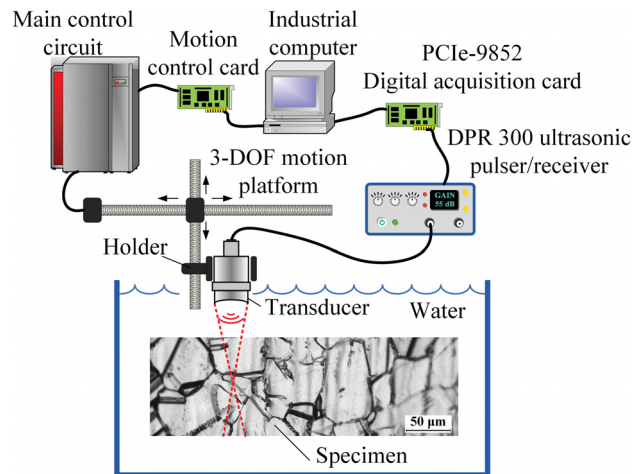

FIG. 1. (Color online) The immersion scanning system with a configuration for normally incident longitudinal-to-longitudinal scattering measurement.

TABLE I. The parameters for focused transducers and the corresponding dimensionless longitudinal wavenumbers and the scattering mean free path. The spot size or $-6\,dB$ beam diameter is estimated as $BD(-6\,dB) = 1.02Fc/fD$, where F is the focal length in water, c is the wave speed in material, f_c is the central frequency, and D is the element diameter (Ref. 33).

No.	Central frequency (MHz)	Focal length in water (mm)	Element diameter (mm)	Spot size in material (mm)	$k_L\bar{d}$	Mean free path (mm)
A	14.04	77.01	12.70	0.65	0.68	7.21 ± 0.29
B	10.20	77.22	12.70	0.90	0.49	19.93 ± 0.99
C	7.11	75.79	12.70	1.27	0.34	69.84 ± 3.26
D	4.83	75.51	12.70	1.87	0.23	294.3 ± 12.6

than each of the mean free paths to reduce the impacts of multiple scattering further. An offset distance of 20 mm from the specimen edge was kept to avoid spurious edge effects. Figure 2 shows the B-scan images and the corresponding spatial average curves $\langle V(t) \rangle$ and third-order moment curves $\langle V^3(t) \rangle$ for each transducer used (A–D). It is emphasized that the operators $\kappa_{\mathbf{xx'}}$ are used, so that the waveforms are aligned as seen in Fig. 2. The numbers of vertical stripes increase because of the longer temporal pulse duration for the lower-frequency transducers. The time gates used for calculating SCC curves are shown in red and have lengths of 3 μs. The backscattering signal found near the red gated region is seen to be highly dependent on the transducer (frequency) used. The grain noise appears more regular (less random) for successively smaller frequencies.

The spatial average of the backscattering signals $\langle V(t) \rangle$ grow with the decrease of $k_L\bar{d}$. The reason why there is non-zero $\langle V(t) \rangle$ resulting from reflections from non-stochastic features, however, it is difficult to discern exactly what is contributing. It may come from the transducer bias, the macroscopic anisotropy, or the microstructure that is not statistically uniform over the region scanned. However, these reasons cannot explain the frequency dependency well. As $0.1 < k_L\bar{d} < 1$, the scattering events are located within the transition between low-frequency Rayleigh and stochastic scattering. The cause of $\langle V(t) \rangle$ is likely associated with the scattering regime, but it is beyond the scope of this paper. The shapes of $\langle V^3(t) \rangle$ are different from those of $\langle V(t) \rangle$. The higher-order $\langle V^{2n-1}(t) \rangle$ have similar behaviors to $\langle V(t) \rangle$ and $\langle V^3(t) \rangle$.
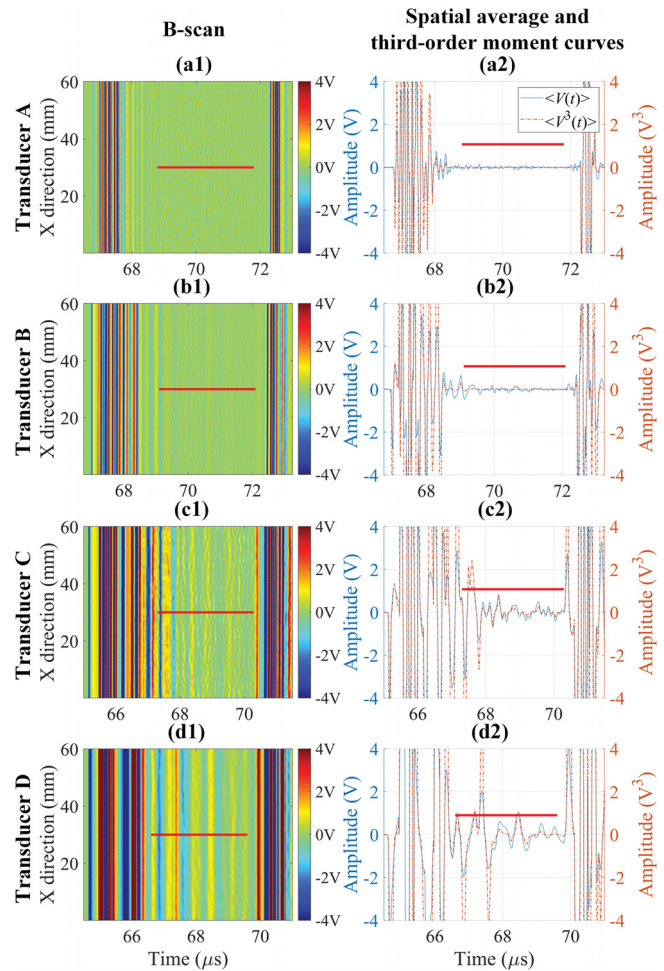

FIG. 2. (Color online) B-scan images and the corresponding spatial average and third-order moment curves after the alignment operation. (a1)–(d1) The B-scan images using transducer A to D. (a2)–(d2) The spatial average curves using transducer A to D. The red lines indicate the time gate used for calculating SCC. Note that the amplitude ranges of (a1)–(b2) are different from those of (c1)–(d2).

B. SCC without time lag

The SCC values without Time Lag can be calculated based on the aligned waveforms. Figures 3(a1)–3(d1) are the zeroth-order matrices $SCC(\tau = 0 | V_{\mathbf{x}}, V_{\mathbf{x'}})$, showing the relationship between each pair of the backscattering signal within the time gate. The SCC matrix is symmetric, and it is
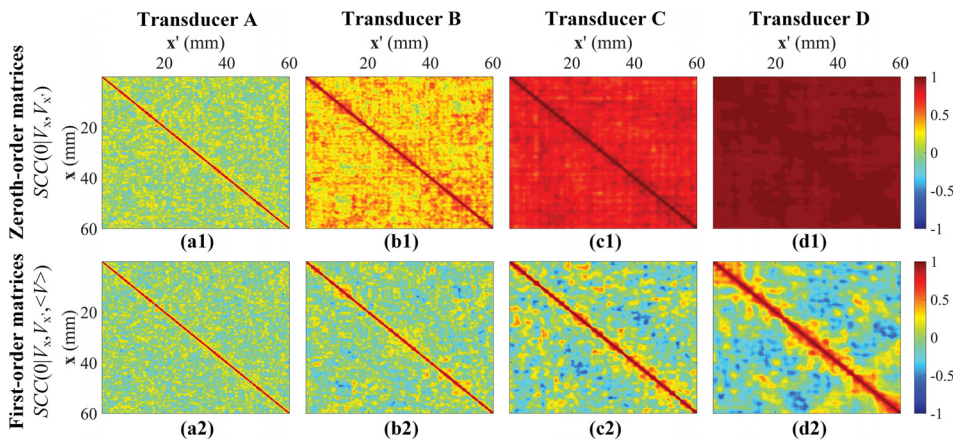

FIG. 3. (Color online) The zeroth- and first-order SCC matrices. (a1)–(d1) zeroth-order matrices $SCC(0|V_{\mathbf{x}},V_{\mathbf{x'}})$ using transducer A to D. (a2)–(d2) first-order matrices $SCC(0|V_{\mathbf{x}},V_{\mathbf{x'}},\langle V \rangle)$ using transducer A to D.

J. Acoust. Soc. Am. **147** (2), February 2020

Song *et al.*   761

a band matrix whose main diagonal corresponds to identical waveforms at $\mathbf{x} = \mathbf{x}'$ and, thus, equal to 1. Even when the separation distance between waveforms is 60 mm, Fig. 3(d1) indicates a strong correlation with SCC above 0.9. The strong correlation at large separation distance indicates that the spatial average is dominating the correlation over the microstructural heterogeneity. Thus, it is demonstrated that the traditional zeroth-order SCC includes more than microstructural effects on the signals. However, the calculation of the first-order matrices $SCC(0|V_{\mathbf{x}}, V_{\mathbf{x}'}, \langle V \rangle)$ seen in Figs. 3(a2)–3(d2) does show a decrease in correlation as a function of separation distance even when $\langle V(t) \rangle$ is dominant. Comparisons from the results in Fig. 3 are highly qualitative. Next step is to quantify the effects of $\langle V(t) \rangle$ and the resultant correlation estimates.

To illustrate the role of high-order SCC quantitatively, the SCC curves at $\tau = 0$ can be calculated as a function of lateral separation $|\mathbf{x} - \mathbf{x}'|$. At a specific lateral separation $|\mathbf{x} - \mathbf{x}'|$, there are many pairs of signals as shown in Fig. 3. Therefore, to minimize error, the average value of SCC is calculated from 150 random pairs of signals for each lateral separation. The results for the traditional and present SCC curves are shown in Fig. 4. One zeroth-order SCC [Eq. (1)], two first-order SCC [Eq. (3)], and one second-order SCC [Eq. (4)] are compared.

For the high frequency transducer A, there is $\langle V(t) \rangle \approx 0$, so that the zeroth-order SCC is close to the higher-order SCC curves. However, with the decease of frequency for transducers B–D, the zeroth-order SCC tends to significantly deviate from the others. When $\langle V(t) \rangle$ displays a large value as seen in Fig. 2(d2), the variation of SCC curves is dramatic as seen in Fig. 4(d). The effect of $\langle V^3 \rangle$ on $SCC(0||\mathbf{x} - \mathbf{x}'|, \langle V^3 \rangle)$ are weaker than those of $\langle V \rangle$ on $SCC(0||\mathbf{x} - \mathbf{x}'|, \langle V \rangle)$. This is supported by the closeness between $SCC(0||\mathbf{x} - \mathbf{x}'|, \langle V \rangle)$ and $SCC(0||\mathbf{x} - \mathbf{x}'|, \langle V \rangle, \langle V^3 \rangle)$. Even though the first- and second-order SCC curves closely agree, it is believed to be important to check the second-order curve before deciding to truncate at
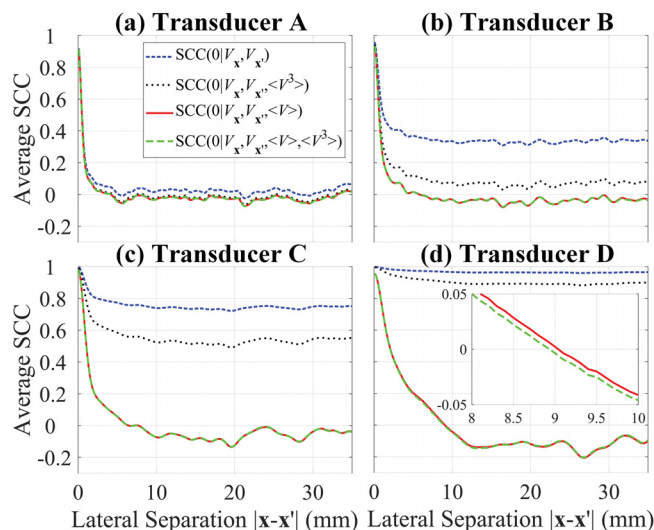
TABLE II. The average ℓ_1-norm between SCC curves without time lag (30 realities for each transducer). The units are both 1.

No.	$SCC(0\|\|\mathbf{x}\text{-}\mathbf{x}'\|)$ vs $SCC(0\|\|\mathbf{x}\text{-}\mathbf{x}'\|, \langle V \rangle, \langle V^3 \rangle)$	$SCC(0\|\|\mathbf{x}\text{-}\mathbf{x}'\|, \langle V^3 \rangle)$ vs $SCC(0\|\|\mathbf{x}\text{-}\mathbf{x}'\|, \langle V \rangle, \langle V^3 \rangle)$	$SCC(0\|\|\mathbf{x}\text{-}\mathbf{x}'\|, \langle V \rangle)$ vs $SCC(0\|\|\mathbf{x}\text{-}\mathbf{x}'\|, \langle V \rangle, \langle V^3 \rangle)$
A	0.04572 ± 0.00011	0.00805 ± 0.00005	0.00132 ± 0.00004
B	0.36116 ± 0.00021	0.10376 ± 0.00015	0.00133 ± 0.00002
C	0.76006 ± 0.00052	0.55937 ± 0.00044	0.00097 ± 0.00002
D	0.97589 ± 0.00055	0.91210 ± 0.00052	0.00362 ± 0.00006

the first-order. The differences between two SCC curves are given by the average ℓ_1-norm $\bar{\ell}_1(\mathbf{A}, \mathbf{B}) = (1/n) \sum_{i=1}^{n} |A_i - B_i|$ where $\mathbf{A}$ and $\mathbf{B}$ are two different. Good convergence performances of first-order SCC are shown in Table II. There are minimal deviations between the first- and second- order SCC as seen in the last column of Table II. Thus, the first-order SCC without time lag appears promising for application.

C. SCC with time lag

Equations (1), (3), and (4) are spatial correlation coefficients defined in a cross-correlation form, which permits observing temporal or phase effects on the SCC. Moreover, the influences of partial correlation analysis on the time lag should be considered. For example, Fig. 5 shows a comparison between $SCC(\tau|V_{\mathbf{x}}, V_{\mathbf{x}'})$ and $SCC(\tau|V_{\mathbf{x}}, V_{\mathbf{x}'}, \langle V \rangle)$ using transducer D. In this example, a pair of waveforms denoted as $V_{\mathbf{x}}$ and $V_{\mathbf{x}'}$ is used with separation $|\mathbf{x} - \mathbf{x}'|$ chosen as 30 mm. The strong correlations present in $SCC(\tau|V_{\mathbf{x}}, V_{\mathbf{x}'})$ result from non-random effects in the signals, the $\langle V(t) \rangle$ influence. Including the effects of $\langle V(t) \rangle$ in the correlation $SCC(\tau|V_{\mathbf{x}}, V_{\mathbf{x}'}, \langle V \rangle)$ produces an SCC that contains weaker correlations, which more closely resemble what one would expect from a random microstructure.

Matrices of the maximum time lag $\tau_{\max}$ from the zeroth-order SCC are shown in Figs. 6(a1)–6(d1) and from the first-order SCC in Figs. 6(a2)–6(d2). The matrices of $\tau_{\max}(V_{\mathbf{x}}, V_{\mathbf{x}'})$ and $\tau_{\max}(V_{\mathbf{x}}, V_{\mathbf{x}'}, \langle V \rangle)$ are skew-symmetric with zeros on the main diagonal. The skew-symmetric features are caused by the relativity of time lag and time lead. In Figs. 6(a1)–6(d1), the fluctuation decreases as the central frequency of transducer decreases. The standard deviation
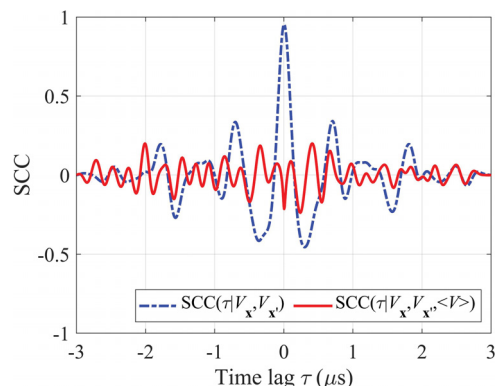

FIG. 4. (Color online) The relationships between the traditional SCC curves and present SCC curves (a)–(d) using transducer A to D.

FIG. 5. (Color online) Comparison between the zeroth- and first-order spatial cross-correlation (transducer D).
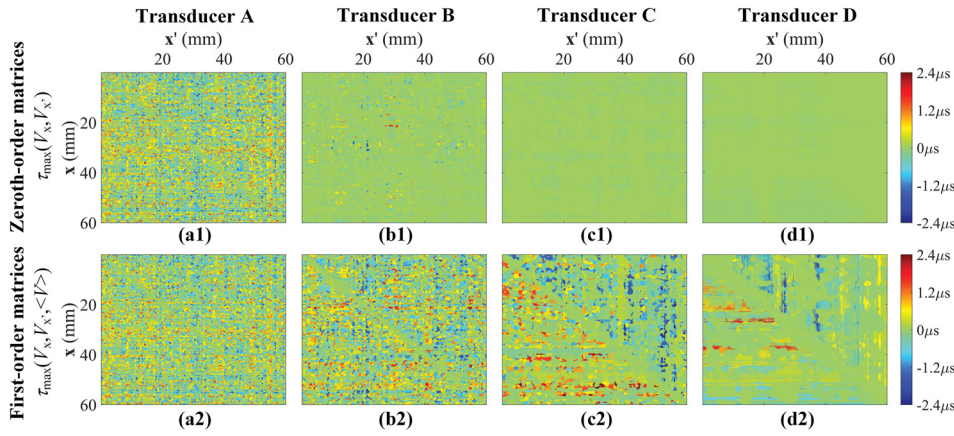
Song *et al.*

FIG. 6. (Color online) The matrices of the zeroth- and first-order maximum time lag. (a1)–(d1) Zeroth-order, using transducer A to D. (a2)–(d2) First-order, using transducer A to D.

values of Figs. 6(a1)–6(d1) are 0.6150, 0.1492, 0.0071, and 0.0039 μs, respectively. This suggests the signals have a fixed phase when using $\tau_{\max}(V_{\mathbf{x}}, V_{\mathbf{x}'})$. However, in Figs. 6(a2)–6(d2), the standard deviation values are 0.6163, 0.6438, 0.5815, and 0.3739 μs, respectively. The randomness of phase increases significantly when considering $\tau_{\max}(V_{\mathbf{x}}, V_{\mathbf{x}'}, \langle V \rangle)$. This result is a reasonable expectation because it follows the "white noise" assumption of the random mirror approach from Fink and his co-workers,[12,23,24] and the "random phase" assumption of the independent scattering model from Thompson and his co-workers.[1,8,34]

Since the matrix of $\tau_{\max}$ is skew-symmetric, the magnitude of the time shift is observed, which is the absolute value of either the time lag or lead time. Similarly, the MTS curve is a function of lateral separation $|\mathbf{x} - \mathbf{x}'|$. Figure 7 shows the MTS curves, including $|\tau_{\max}(|\mathbf{x} - \mathbf{x}'|)|$, $|\tau_{\max}(|\mathbf{x} - \mathbf{x}'|, \langle V^3 \rangle)|$, $|\tau_{\max}(|\mathbf{x} - \mathbf{x}'|, \langle V \rangle)|$, and $|\tau_{\max}(|\mathbf{x} - \mathbf{x}'|, \langle V \rangle, \langle V^3 \rangle)|$. The results show that the MTS curves resemble sigmoid functions. Thus, they are divided in stage I, II, and III, where the curves are nearly stable at stage III and stage I as seen in the insets of Figs. 7(b) and 7(c), and a sharp transition stage II is generally present between the initial and final stages. When

the central frequency decreases, the stage I lengthens, the slope of stage II decreases, and the arrival of stage III postpones consequently. Meanwhile, the stable value of stage III decreases. For the zeroth-order case, the $|\tau_{\max}(|\mathbf{x} - \mathbf{x}'|)|$ is a sigmoid function when transducer A or even B is used. However, the initial stage tends to be reduced at low frequency. The first- and second-order curves always keep the feature of Stage I well. The convergence properties are given in Table III, using the average l_1-norm between the MTS curves. The first- and second-order MTS curves matches with each other as expected (<0.02 μs).

D. Effects of experimental conditions on SCC

The experimental conditions can affect the statistics of spatial cross-correlation in many aspects. Here, concern the effects of signal alignment and the sampling rate on the SCC. First, Figs. 8(a)–8(c) show the B-scan images of transducer D under different alignment conditions. Set the alignment operator as $\kappa_{\mathbf{xx}'}$, 0, and $-3\kappa_{\mathbf{xx}'}$, respectively. It can be seen in Fig. 8(b) that the signals are slightly unaligned without using $\kappa_{\mathbf{xx}'}$, but this happens naturally. The top and bottom surfaces of the specimen might be rough and nonparallel, and the transducer might not be perfectly normal. By contrast, there is an artificial nonalignment in Fig. 8(c). The maximum offsets of the front-wall echo in Figs. 8(a)–8(c) are 0.00, 0.08, and 0.20 μs, respectively. Then, Fig. 8(d) shows the spatial average curves $\langle V(t) \rangle$ under these three conditions. The spatial average curves are degenerated in the case without using $\kappa_{\mathbf{xx}'}$ and using $-3\kappa_{\mathbf{xx}'}$.

The zeroth- and first-order curves $SCC(0||\mathbf{x} - \mathbf{x}'|)$ and $SCC(0||\mathbf{x} - \mathbf{x}'|, \langle V \rangle)$, and the MTS curves $|\tau_{\max}(|\mathbf{x} - \mathbf{x}'|)|$ and $|\tau_{\max}(|\mathbf{x} - \mathbf{x}'|, \langle V \rangle)|$ under different alignment
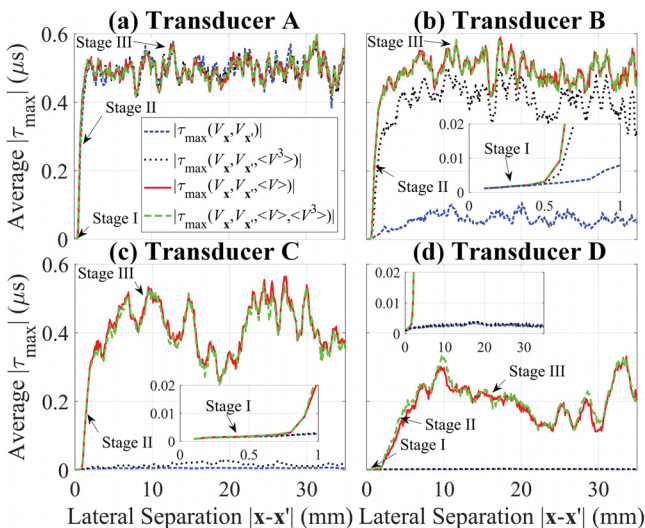

FIG. 7. (Color online) The relationships between the traditional MTS curves and present MTS curves (a)–(d) using transducer A to D.

TABLE III. The average ℓ_1-norm between the MTS curves (30 realities for each transducer). The units are both μs.

No.	$\|\tau_{\max}(\|\mathbf{x}\text{-}\mathbf{x}'\|)\|$ vs $\|\tau_{\max}(\|\mathbf{x}\text{-}\mathbf{x}'\|, \langle V \rangle, \langle V^3 \rangle)\|$	$\|\tau_{\max}(\|\mathbf{x}\text{-}\mathbf{x}'\|, \langle V^3 \rangle)\|$ vs $\|\tau_{\max}(\|\mathbf{x}\text{-}\mathbf{x}'\|, \langle V \rangle, \langle V^3 \rangle)\|$	$\|\tau_{\max}(\|\mathbf{x}\text{-}\mathbf{x}'\|, \langle V \rangle)\|$ vs $\|\tau_{\max}(\|\mathbf{x}\text{-}\mathbf{x}'\|, \langle V \rangle, \langle V^3 \rangle)\|$
A	0.0204 ± 0.0007	0.0127 ± 0.0005	0.0109 ± 0.0006
B	0.4185 ± 0.0016	0.0825 ± 0.0012	0.0113 ± 0.0004
C	0.3866 ± 0.0018	0.3773 ± 0.0018	0.0156 ± 0.0005
D	0.1861 ± 0.0012	0.1859 ± 0.0012	0.0145 ± 0.0004

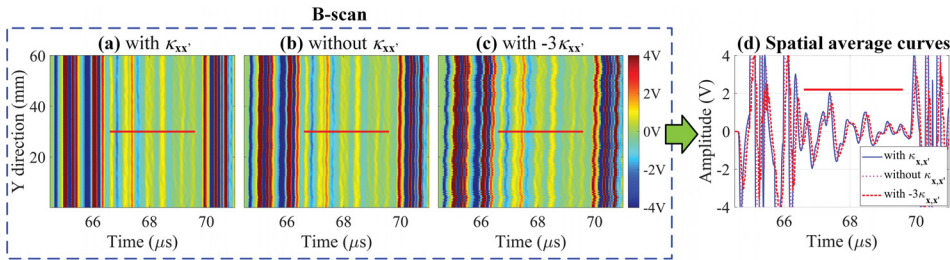J. Acoust. Soc. Am. **147** (2), February 2020

Song *et al.* 763

FIG. 8. (Color online) B-scan images of transducer D under different alignment conditions. (a) With $\kappa_{xx'}$, (b) without $\kappa_{xx'}$, (c) with $-3\kappa_{xx'}$, (d) corresponding spatial average curves of panels (a) to (c).

conditions are shown in Fig. 9. When signals become unaligned, the zeroth-order SCC curves decrease and the zeroth-order $|\tau_{max}|$ curves become greater, since the back-scattering signals now have additional incongruences. The fluctuation levels also become increased and several humps appear. However, our specimen just has one length scale. Thus, the humps should correspond to the level of misalignment. Unfortunately, higher-order SCC and $|\tau_{max}|$ does not overcome the misalignment. One of the reasons is that higher-order statistics are sensitive to the spatial average curves. Thus, the alignment operator for in Eq. (1) is crucial for the spatial average curve and the statistics of high-order SCC.

It is also interesting to show the effects of the sampling rate on measured correlations. Consider the waveform data from transducer D after signal alignment. An excessive sampling rate of 200 MHz for a 4.83 MHz (nominally 5 MHz) transducer will produce redundant data in time domain. Let F_s be the sampling rate of the discrete acquisition. Thus, each waveform is resampled at $F_s = 50$, 20, and 10 MHz sampling rate, respectively. The time gates used in the analysis remain 3 μs. Consequently, the number of discrete sampling points within the gate are reduced from 600 to 150, 60, and 30 sampling points, respectively.

In Fig. 10, a comparison between $SCC(0||\mathbf{x} - \mathbf{x}'|)$, $|\tau_{max}(|\mathbf{x} - \mathbf{x}'|)|$, $SCC(0||\mathbf{x} - \mathbf{x}'|, \langle V \rangle)$, and $|\tau_{max}(|\mathbf{x} -\mathbf{x}'|, \langle V \rangle)|$ for the different sampling rates is given. When

the sampling rate is greater than 20 MHz, the SCC curves agree with each other. However, when the sampling rate is 10 MHz, discrepancies appear. The discrepancy results from the sampling rates inability to cover the bandwidth of transducer D, whose -6 dB bandwidth is from 3.03 to 6.62 MHz (74.3% bandwidth). However, the zero-order MTS curves are deeply dependent on the sampling rate as shown in Fig. 10(b) and its inset. When the sampling rate is 10 or 20 MHz, $|\tau_{max}(|\mathbf{x} - \mathbf{x}'|)|$ are almost zero. The reason might be that the fluctuations of $|\tau_{max}(|\mathbf{x} - \mathbf{x}'|)|$ is much smaller than the sampling interval $\Delta t_s = 1/F_s$, when using transducer D and there are non-zero $\langle V(t) \rangle$. Actually, the fluctuations are only $\sim$0.003 μs, but the sampling intervals are $\Delta t_s = 0.020$, 0.050, 0.100 μs when $F_s = 50$, 20, and 10 MHz, respectively. Therefore, when using low sampling rate, the temporal resolutions are not enough to measure these fluctuations. Contrarily, the first-order MTS curves that have the magnitudes $\sim$0.300 μs are nearly not affected by the sampling rate until it is lower than 20 MHz as shown in Fig. 10(d).

From Fig. 10, it is evident that the 200 MHz sampling rate does produce redundant data points, especially for calculating the first-order SCC curves and MTS curves. The reason why taking the sampling rate into account is that the redundancy influences the independent data assumption in Eq. (6). Thus, the degrees of freedom in the time domain should be reduced. This reduction in degrees of freedom impacts the Student's t-test when calculating the UTD
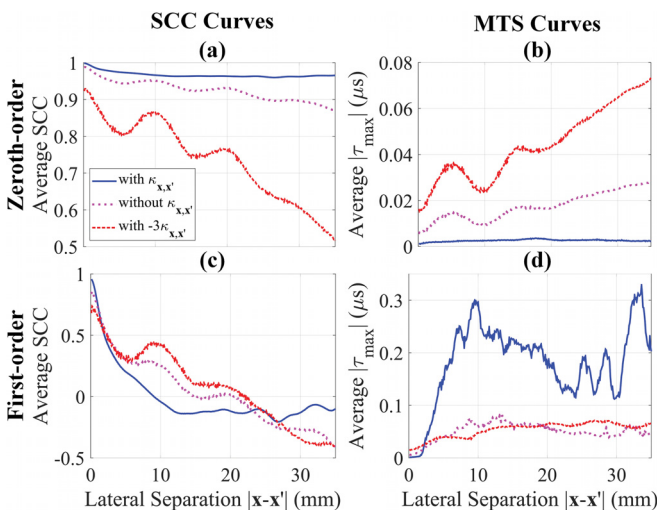

FIG. 9. (Color online) The effects of signal alignment on zeroth- and first-order SCC curves and MTS curves. (a) $SCC(0||\mathbf{x}-\mathbf{x}'|)$, (b) $|\tau_{max}(|\mathbf{x}-\mathbf{x}'|)|$, (c) $SCC(0||\mathbf{x}-\mathbf{x}'|,\langle V\rangle)$, (d) $|\tau_{max}(|\mathbf{x}-\mathbf{x}'|,\langle V\rangle)|$.
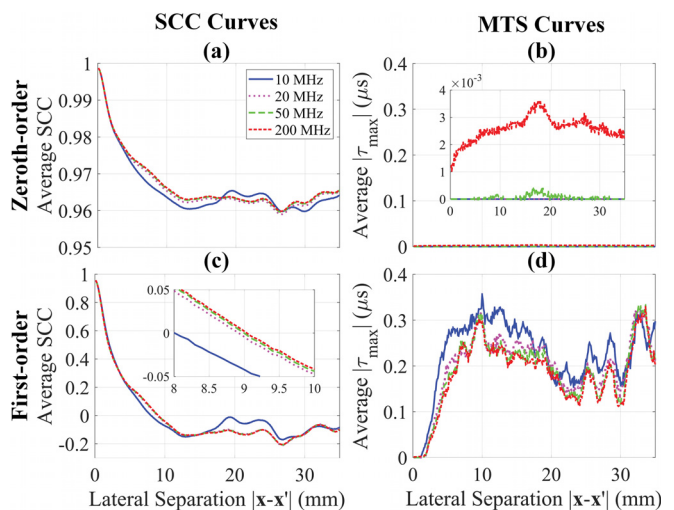

FIG. 10. (Color online) The influences of the sampling rate on the zero- and first-order SCC and MTS curves. (a) $SCC(0||\mathbf{x}-\mathbf{x}'|)$, (b) $|\tau_{max}(|\mathbf{x}-\mathbf{x}'|)|$, (c) $SCC(0||\mathbf{x}-\mathbf{x}'|,\langle V\rangle)$, (d) $|\tau_{max}(|\mathbf{x}-\mathbf{x}'|,\langle V\rangle)|$.
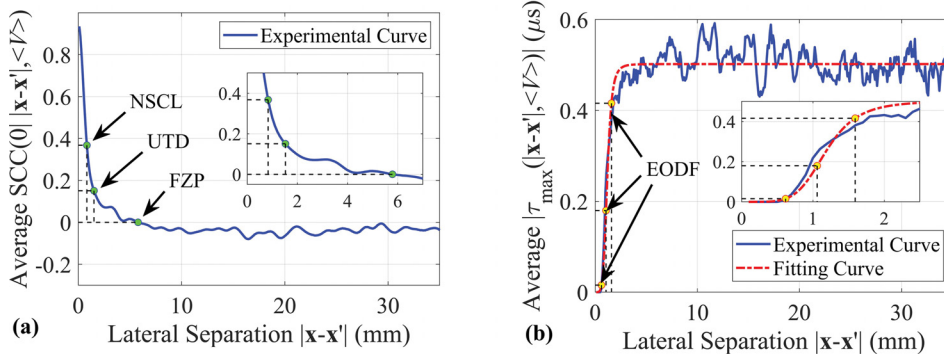
FIG. 11. (Color online) The first-order SCC curve and the least square fitting of MTS curve (using transducer B) and different kinds of indicators. (a) $SCC(0\|\mathbf{x}-\mathbf{x}'\|,\langle V\rangle)$, (b) $|\tau_{\max}(\|\mathbf{x}-\mathbf{x}'\|,\langle V\rangle)|$.

indicator. In terms of Fig. 10, a factor of 4 compared to the central frequency of each transducer is applied to choose the sampling rate.

E. Indicator analysis for application

A total of six indicators in four categories are proposed to evaluate the first-order SCC curve and the MTS curve. Considering the backscattering data from transducer B as an example, $SCC(0\|\mathbf{x}-\mathbf{x}'\|,\langle V\rangle)$ and the least square fitting of $|\tau_{\max}(\|\mathbf{x}-\mathbf{x}'\|,\langle V\rangle)|$ are shown in Fig. 11, and the indicators of these two kinds of curve are also shown. The NSCL value is determined by the intersection of the first-order SCC curve and the line $SCC = 1/e = 0.368$. To obtain the UTD value, $\alpha = 95\%$ is set to calculate the upper bound, and the intersection of the first-order SCC curve and the upper bound gives the UTD. In the same way, the first intersection of the first-order SCC curve and the positive axis give the FZP. Their exact values are given by the spline interpolation. Note that the NSCL, UTD, and FZP values are extracted from the experimental curve, whereas the EODFs are extracted from the fitting curve using the Eq. (11).

Furthermore, the results of indicators analysis are shown in Table IV. The indicators of $SCC(0\|\mathbf{x}-\mathbf{x}'\|,\langle V\rangle)$ and $|\tau_{\max}(\|\mathbf{x}-\mathbf{x}'\|,\langle V\rangle)|$ work well even when the spatial average curves are dominant. It can be seen that the NSCLs are comparable to the $-6\,\mathrm{dB}$ beam diameter (in Table I, except for the case using transducer D.

The UTDs are almost twice the NSCLs, as $\alpha = 95\%$. The FZPs are the longest, but they are all less than the element diameters of the transducer, not to mention the mean free paths (in Table I. The first EODFs are the smallest, and second EODFs and third EODFs are comparable to the NSCLs and UTDs, which shows the self-consistency of this paper. Meanwhile, the indicators analysis of the zeroth-order SCC curves and the MTS curves are also shown in Table IV. However, the indicators analysis of $SCC(0\|\mathbf{x}-\mathbf{x}'\|)$ and $|\tau_{\max}(\|\mathbf{x}-\mathbf{x}'\|)|$ fail in most of the cases. For transducer B, NSCL is the remaining indicator that can be obtained from zeroth-order SCC, but it is 6.79 times larger than the one from first-order SCC.

To this point, a set of quantitative indicators have been given to analyze the SCC curve and MTS curve. Now, they are compared in a practical application. As an example, these indicators can be utilized to help guide experimental backscattering measurements based on spatial variance curves. Such measurements have been used previously to evaluate the grain size[1–3] and detect microflaws.[4–6] A spatial variance curve can be given by

$$\Phi(t) = \frac{1}{N}\sum_{i=1}^{N}\left[V_i^2(t)\right] - \left[\frac{1}{N}\sum_{i=1}^{N}V_i(t)\right]^2. \quad (12)$$

Different spatial variance curves are calculated with the lateral separations that come from the rounded-off values of

TABLE IV. The results indices analyses. The sign "—" in the table means that this computation fails. Zeroth-order means $SCC(0\|\mathbf{x}-\mathbf{x}'\|)$ and first-order means $SCC(0\|\mathbf{x}-\mathbf{x}'\|,\langle V\rangle)$. The upper bounds are 0.123, 0.151, 0.174, and 0.214, for transducer A to D, respectively.

No.	NSCL (mm) Zeroth-order	NSCL (mm) First-order	UTD (mm) Zeroth-order	UTD (mm) First-order	FZP (mm) Zeroth-order	FZP (mm) First-order
A	0.633	0.601	1.483	1.094	5.327	3.878
B	5.663	0.834	—	1.523	—	5.791
C	—	1.348	—	2.430	—	6.508
D	—	2.916	—	4.687	—	8.926

No.	First EODF (mm) Zeroth-order	First EODF (mm) First-order	Second EODF (mm) Zeroth-order	Second EODF (mm) First-order	Third EODF (mm) Zeroth-order	Third EODF (mm) First-order
A	0.426	0.383	0.732	0.657	1.100	0.988
B	—	0.618	—	1.060	—	1.593
C	—	0.893	—	1.532	—	2.302
D	—	1.834	—	3.148	—	4.730

NSCL, UTD, FZP, EODF1, EODF2, and EODF3, and they are denoted as $\Phi^{NSCL}(t)$, $\Phi^{UTD}(t)$, $\Phi^{FZP}(t)$, $\Phi^{EODF1}(t)$, $\Phi^{EODF2}(t)$, and $\Phi^{EODF3}(t)$, respectively. Transducer B is still used for the comparation here, and each spatial variance curve is given by 11 waveforms (limited by the size of the specimen and a largest lateral separation as 5.8 mm). To evaluate the equivalency of two variance curves, the F-test for the ratio curve of variance is recommend.[35] The upper bound and lower bound of the ratio curve in Figs. 12(a2)–12(e2) are given by the F-test. When the following condition is true, the F-test is passed

$$\Pr\left\{ F_{\frac{1-\alpha'}{2}}(N_A - 1, N_B - 1) < \frac{\Phi^A(t)}{\Phi^B(t)} \right.$$
$$\left. \leq F_{\frac{1+\alpha'}{2}}(N_A - 1, N_B - 1) | t_0 < t \leq t_1 \right\} \geq \alpha', \quad (13)$$

where the superscripts A and B are the kinds of the lateral separations, and N_A and N_B are the corresponding number of waveforms. α' is the confidence level of the F-test. Equation (13) means when the probability that the ratio curve selected by the time gate comes within the bounds is larger than the confidence level, one can judge that $\Phi^A(t) \Longleftrightarrow \Phi^B(t)$ in a statistical sense. Two additional points are highlighted, (1) the precondition for the F-test is that the waveforms used to calculate these two variance curves are independent; (2) $\Phi^A(t)$ and $\Phi^B(t)$ approach to the same value of population variance when $N_A \rightarrow \infty$ and $N_B \rightarrow \infty$, because the specimen is assumed statistically homogeneous and has a consistent grain size. Therefore, when N_A and N_B are not sufficiently large, the difference between $\Phi^A(t)$ and $\Phi^B(t)$ can be ascribed to the dependence of the data.

The confidence level α' of the F-test is set as 95%, and the numbers of waveforms are $N_A = N_B = 11$. The largest lateral separation FZP is used as the reference by setting the denominator as $\Phi^B(t) = \Phi^{FZP}(t)$. Figure 12 shows the spatial variance curves $\Phi(t)$ with different kinds of lateral separations and their ratios. There are no intuitive deviations between two spatial variance curves in Figs. 12(a1)–12(e1). However, the probabilities about the ratio curve in Eq. (13) are measured as 94.3%, 96.2%, 92.8%, 94.8%, and 98.0% under the lateral separation conditions using NSCL, UTD, EODF1, EODF2, and EODF3, respectively. Thus, the F-tests are passed when using UTD or EODF3 as the lateral separation. Then, we have $\Phi^{UTD}(t) \Longleftrightarrow \Phi^{FZP}(t)$ and $\Phi^{EODF3}(t) \Longleftrightarrow \Phi^{FZP}(t)$. In other words, if the scanning step is larger than a limit, the finally obtained $\Phi(t)$ are always equivalent and using larger scanning step cannot supply more information for calculating $\Phi(t)$. Since UTD and EODF3 are nearly smaller than half of FZP, it is more convenient to measure $\Phi^{UTD}(t)$ and $\Phi^{EODF3}(t)$ than $\Phi^{FZP}(t)$, particularly when the size of specimen is small. Thus, the UTD and EODF3 are good estimations for the smallest scanning step in the ultrasonic scattering measurement to get uncorrelated backscattering signal. Notice also that since the NSCL from zero-order SCC ($\sim$5.7 mm) is close to the FZP from first-order SCC ($\sim$5.8 mm) in our case, the zeroth-order SCC overestimates the scanning step obviously.

Additionally, to illustrate the relationship between the loss of correlation and the lateral separation given by the rounded-off values of the indicators, the backscattering signals from transducer B are shown in Fig. 13(a). The reference signal in blue is from transducer position **x**, and the signal in red is from varying transducer position **x**′ based on different indicators. The dotted line in black is the spatial average curve $\langle V(t) \rangle$. It can be seen that there is an average tendency before 69.5 μs, and the all signals follow this tendency. However, taking the average curve as a middle line, the variations are significant when using UTD, or EODF3,
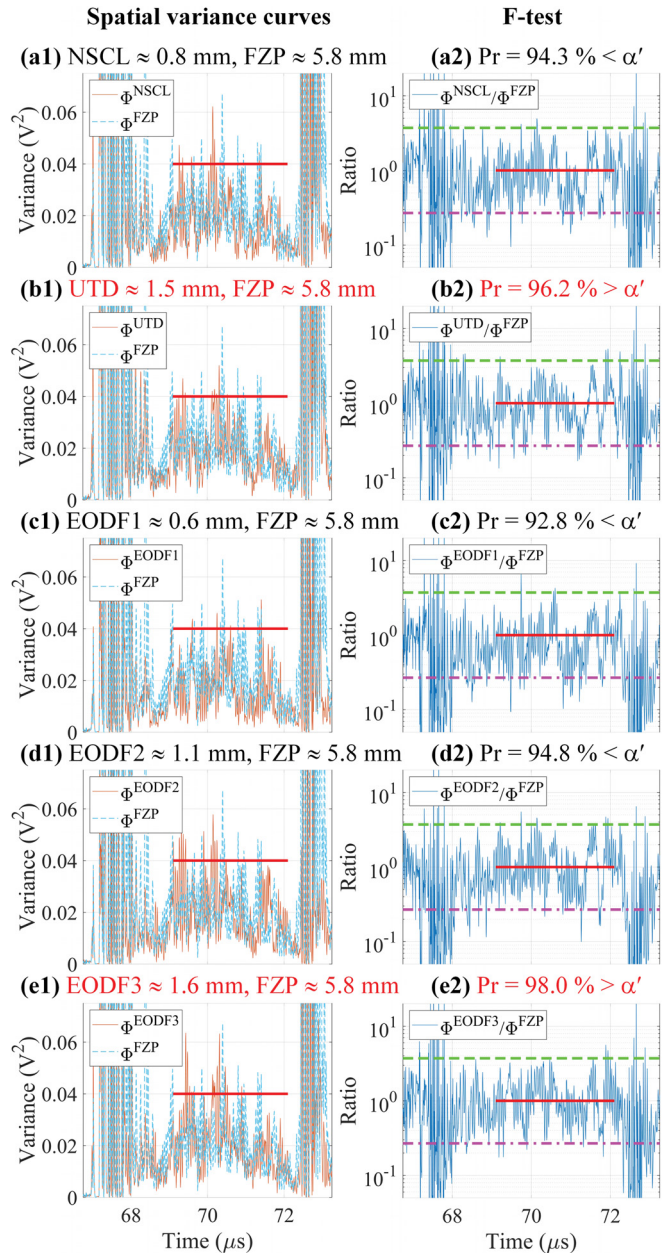

FIG. 12. (Color online) The spatial variance curves with different kinds of lateral separations and their ratios. The red lines are the gates. The green dashed lines and the purple dashed-dotted lines are corresponding to the upper bounds $F_{0.975}(10,10)$ and the lower bounds $F_{0.025}(10,10)$. (a1, a2) Φ^{NSCL} and Φ^{FZP}, and their ratio (b1, b2) Φ^{UTD} and Φ^{FZP}, and their ratio (c1, c2) Φ^{EODF1} and Φ^{FZP}, and their ratio (d1, d2) Φ^{EODF3} and Φ^{FZP}, and their ratio (e1, e2) Φ^{EODF3} and Φ^{FZP}, and their ratio.

or FZP. Especially, for FZP, two signals are almost ortho-metric compared with the average curve as $SCC(0|V_{\mathbf{x}}, V_{\mathbf{x}'}, \langle V \rangle) = -0.039$. But Fig. 12 shows it is enough to say two signals are statistically uncorrelated when using UTD and EODF3.

Figure 13(b) shows the effects of time shift on the correlations based on transducer B and FZP. Not only the red line is shifted, but also the black line is shifted to get the partial cross-correlation coefficient. With a -0.2 μs time lag, two signals are negatively correlated and the zero-order SCC meets its maximum amplitude; with a -0.4 μs time lag, two signals are positively correlated and the first-order SCC meets it maximum amplitude.

IV. SUMMARY

In this paper, the partial cross-correlation analysis in statistics is introduced to calculate the spatial correlation coefficient of ultrasonic backscattering signals. The SCC is generalized from zeroth-order to any higher-order case to include the effects of confounding variables. Moreover,

several indicators are defined to quantify the SCC curve without time lag and the maximum time shift (MTS) curve. They are used in ultrasonic applications to reveal the smallest spatial scanning step during scattering measurements that leads to uncorrelated backscattering signals.

For the experimental configuration considered, the results show that the first-order SCC converges to the second-order SCC well. Thus, the spatial average curve is the leading order of the odd-order moments. However, it is recommended that, in general, the higher-order SCC should be checked before deciding to truncate. The effects of experimental conditions on the SCC are also shown. To get a valid measure of the SCC, the waveforms should be aligned. The SCC and MTS curves broke down even for a variation of the front-wall echo as small as 0.08 μs. Additionally, the required sampling rate is modest to measure the SCC and MTS curves. In the investigated cases, sampling rates as low as 4× the central frequency were able to resolve accurate SCC and MTS curves.

Finally, the indicator analysis shows that the values of UTD, from Eq. (7), and EODF3, from Eq. (11), are
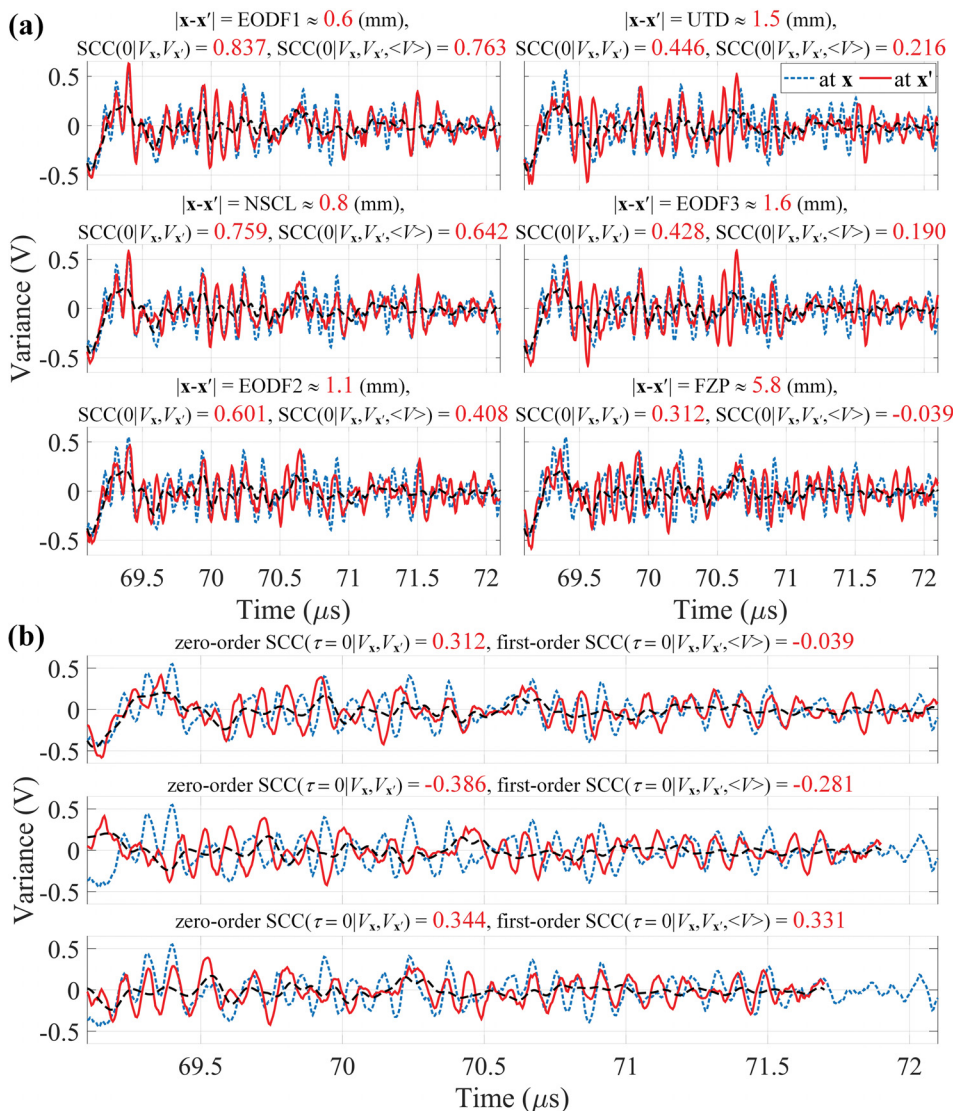

FIG. 13. (Color online) The relationship between the loss of correlation and the lateral separations (a), and the effect of time shift on the correlation (b). The dashed line in black is the spatial average curve $\langle V \rangle$.

approximately equal. However, the UTD is impacted by the confidence level of the Student's t-test. In contrast, EODF3 represents the MTS curve that approaches a stable value after this lateral separation. Both the indicator UTD or EODF3 can answer the fundamental problem of how far two transducer positions should be to receive statistically uncorrelated backscattering signals.

In the future, the smallest size of specimen for microstructural characterization is going to be determined by using the first-order SCC and the indicator UTD or EODF3. In addition, it should be noted that the zeroth-order SCC is of value. The zeroth-order SCC and higher-order SCC can supplement each other to accomplish the same task like microstructural characterization or microflaw detection in the future. The speckle noise within an ultrasonic image[36] may also be interpreted as well.

ACKNOWLEDGMENTS

[1] F. J. Margetan, T. A. Gray, and R. B. Thompson, "A technique for quantitatively measuring microstructurally induced ultrasonic noise," in *Review of Progress in Quantitative NDE*, edited by D. O. Thompson and D. E. Chimenti (Plenum, New York, 1991), Vol. 10, pp. 1721–1728.

[2] L. Yang, J. Li, O. I. Lobkis, and S. I. Rokhlin, "Ultrasonic propagation and scattering in duplex microstructures with application to titanium alloys," J. Nondestruct. Eval. **31**, 270–283 (2012).

[3] G. Ghoshal and J. A. Turner, "Diffuse ultrasonic backscatter at normal incidence through a curved interface," J. Acoust. Soc. Am. **128**, 3449–3458 (2010).

[4] Y. Song, X. Zi, Y. Fu, X. Li, C. Chen, and K. Zhou, "Nondestructive testing of additively manufactured material based on ultrasonic scattering measurement," Measurement **118**, 105–112 (2018).

[5] Y. Song, C. M. Kube, Z. Peng, J. A. Turner, and X. Li, "Flaw detection with ultrasonic backscatter signal envelopes," J. Acoust. Soc. Am. **145**, EL142–EL148 (2019).

[6] Y. Song, J. A. Turner, Z. Peng, C. Chao, and X. Li, "Enhanced ultrasonic flaw detection using an ultra-high gain and time-dependent threshold," IEEE Trans. Ultrason. Ferroelectr. Freq. Control **65**, 1214–1225 (2018).

[7] R. B. Thompson, L. Yu, and F. J. Margetan, "A formal theory for the spatial correlation of backscattered ultrasonic grain noise," in *Review of Progress in Quantitative NDE*, edited by D. O. Thompson and D. E. Chimenti (AIP, Melville, NY, 2005), Vol. 24, pp. 1292–1299.

[8] L. Yu, R. B. Thompson, and F. J. Margetan, "The spatial correlation of backscattered ultrasonic grain noise: Theory and experimental validation," IEEE Trans. Ultrason. Ferroelectr. Freq. Control **57**, 363–378 (2010).

[9] A. Derode, A. Tourin, and M. Fink, "Limits of time-reversal focusing through multiple scattering: Long-range correlation," J. Acoust. Soc. Am. **107**, 2987–2998 (2000).

[10] A. Tourin, A. Derode, A. Peyre, and M. Fink, "Transport parameters for an ultrasonic pulsed wave propagating in a multiple scattering medium," J. Acoust. Soc. Am. **108**, 503–512 (2000).

[11] A. Derode and M. Fink, "Spatial coherence of ultrasonic speckle in composites," IEEE Trans. Ultrason. Ferroelectr. Freq. Control **40**, 666–675 (1993).

[12] A. Derode and M. Fink, "Partial coherence of transient ultrasonic fields in anisotropic random media: Application to coherent echo detection," J. Acoust. Soc. Am. **101**, 690–704 (1997).

[13] S. Li, A. Poudel, and T. P. Chu, "Ultrasonic defect mapping using signal correlation for nondestructive evaluation (NDE)," Res. Nondestructr. Eval. **26**, 90–106 (2015).

[14] R. Cepel, K. C. Ho, B. A. Rinker, D. D. Palmer, T. P. Lerch, and S. P. Neal, "Spatial correlation coefficient images for ultrasonic detection," IEEE Trans. Ultrason. Ferroelectr. Freq. Control **54**, 1841–1850 (2007).

[15] E. Verdet, "Étude sur la constitution de la lumiere non polarisée et de la lumiere partiellement polarisée" ("Study on the constitution of unpolarized light and partially polarized light"), Ann. Sci. E.N.S. **2**, 291–316 (1865).

[16] A. A. Michelson and E. W. Morley, "On the relative motion of the Earth and the luminiferous ether," Am. J. Sci. **34**, 333–345 (1887).

[17] P. H. Van Cittert, "Die wahrscheinliche Schwingungsverteilung in einer von einer Lichtquelle direkt oder mittels einer Linse beleuchteten Ebene" ("The probable distribution of vibrations in a plane illuminated directly by a light source or by means of a lens"), Physica **1**, 201–210 (1934).

[18] P. H. Van Cittert, "Kohaerenz-probleme" ("Coherence problems"), Physica **6**, 1129–1138 (1939).

[19] F. Zernike, "The concept of degree of coherence and its application to optical problems," Physica **5**, 785–795 (1938).

[20] J. W. Goodman, *Statistical Optics*, 2nd ed. (Wiley, New York, 2015), Chap. 5.

[21] E. Wolf, "A macroscopic theory of interference and diffraction of light from finite sources, I. Fields with a narrow spectral range," Proc. R. Soc. London A **225**, 96–111 (1954).

[22] E. Wolf, "A macroscopic theory of interference and diffraction of light from finite sources II. Fields with a spectral range of arbitrary width," Proc. R. Soc. London A **230**, 246–265 (1955).

[23] A. Derode and M. Fink, "The notion of coherence in optics and its application to acoustics," Eur. J. Phys. **15**, 81–90 (1994).

[24] A. Derode and M. Fink, "Correlation length of ultrasonic speckle in anisotropic random media: Application to coherent echo detection," J. Acoust. Soc. Am. **103**, 73–82 (1998).

[25] C. Papadacci, M. Tanter, M. Pernot, and M. Fink, "Ultrasound backscatter tensor imaging (BTI): Analysis of the spatial coherence of ultrasonic speckle in anisotropic soft tissues," IEEE Trans. Ultrason. Ferroelectr. Freq. Control **61**, 986–996 (2014).

[26] D. Kurowicka and R. M. Cooke, "Conditional, partial and rank correlation for the elliptical copula; dependence modelling in uncertainty analysis," in *Proceedings ESREL*, edited by E. Zio, M. Demichela, and N. Piccinini (Politecnico di Torino, Torino, 2001), Vol. 1, pp. 1795–1802.

[27] A. De La Fuente, N. Bing, I. Hoeschele, and P. Mendes, "Discovery of meaningful associations in genomic data using partial correlation coefficients," Bioinformatics **20**, 3565–3574 (2004).

[28] E. Stark, R. Drori, and M. Abeles, "Partial cross-correlation analysis resolves ambiguity in the encoding of multiple movement features," J. Neurophysiol. **95**, 1966–1975 (2006).

[29] N. S. Neidell and M. T. Taner, "Semblance and other coherency measures for multichannel data," Geophysics **36**, 482–497 (1971).

[30] B. Illowsky and S. Dean, *Introductory Statistics* (Rice University, Texas, 2013), Chap. 12.

[31] R. L. Weaver, "Diffusivity of ultrasound in polycrystals," J. Mech. Phys. Solids **38**, 55–86 (1990).

[32] J. A. Turner, "Scattering and diffusion of seismic waves," Bull. Seismol. Soc. Am. **88**, 276–283 (1998).

[33] G. S. Kino, *Acoustic Waves: Devices, Imaging and Analog Signal Processing* (Prentice-Hall, Englewood Cliffs, NJ, 1987), Chap. 3.

[34] I. Yalda, F. J. Margetan, and R. B. Thompson, "Predicting ultrasonic grain noise in polycrystals: A Monte Carlo model," J. Acoust. Soc. Am. **99**, 3445–3455 (1996).

[35] D. Wackerly, W. Mendenhall, and R. L. Scheaffer, *Mathematical Statistics with Applications*, 7th ed. (Thomson Learning, Belmont, CA, 2008), Chap. 10.

[36] R. L. Bevan, J. Zhang, N. Budyn, A. J. Croxford, and P. D. Wilcox, "Experimental quantification of noise in linear ultrasonic imaging," IEEE Trans. Ultrason. Ferroelectr. Freq. Control **66**, 79–90 (2018).